Earth and Planetary Science Letters 472 (2017) 152–163

Contents lists available at ScienceDirect

Earth and Planetary Science Letters

www.elsevier.com/locate/epsl

Paleomagnetic evidence for dynamo activity driven by inward crystallisation of a metallic asteroid

James F.J. Bryson [a,b,*], Benjamin P. Weiss [a], Richard J. Harrison [b], Julia Herrero-Albillos [c,d], Florian Kronast [e]

[a] Department of Earth, Atmospheric and Planetary Sciences, Massachusetts Institute of Technology, Cambridge, MA, USA
[b] Department of Earth Sciences, University of Cambridge, Cambridge, UK
[c] Centro Universitario de la Defensa, Ctra. de Huesca s/n, E-50090 Zaragoza, Spain
[d] Instituto de Ciencia de Materiales de Aragón, CSIC – Universidad de Zaragoza, Pedro Cerbuna 12, E-50009 Zaragoza, Spain
[e] Helmholtz Zentrum Berlin, Elektronenspeicherring BESSY II, Albert-Einstein-Strasse 15, Berlin 12489, Germany

ARTICLE INFO

Article history:
Received 26 January 2017
Received in revised form 13 April 2017
Accepted 17 May 2017
Available online 6 June 2017
Editor: B. Buffett

Keywords:
meteorite paleomagnetism
iron meteorite
cloudy zone
X-ray photoemission electron microscopy
AF demagnetisation
core dynamo activity

ABSTRACT

The direction in which a planetary core solidifies has fundamental implications for the feasibility and nature of dynamo generation. Although Earth's core is outwardly solidifying, the cores of certain smaller planetary bodies have been proposed to inwardly solidify due to their lower central pressures. However, there have been no unambiguous observations of inwardly solidified cores or the relationship between this solidification regime and planetary magnetic activity. To address this gap, we present the results of complimentary paleomagnetic techniques applied to the matrix metal and silicate inclusions within the IVA iron meteorites. This family of meteorites has been suggested to originate from a planetary core that had its overlaying silicate mantle removed by collisions during the early solar system. This process is thought to have produced a molten ball of metal that cooled rapidly and has been proposed to have inwardly solidified. Recent thermal evolution models of such a body predict that it should have generated an intense, multipolar and time-varying dynamo field. This field could have been recorded as a remanent magnetisation in the outer, cool layers of a solid crust on the IVA parent core. We find that the different components in the IVA iron meteorites display a range of paleomagnetic fidelities, depending crucially on the cooling rate of the meteorite. In particular, silicate inclusions in the quickly cooled São João Nepomuceno meteorite are poor paleomagnetic recorders. On the other hand, the matrix metal and some silicate subsamples from the relatively slowly cooled Steinbach meteorite are far better paleomagnetic recorders and provide evidence of an intense ($\gtrsim$100 μT) and directionally varying (exhibiting significant changes on a timescale $\lesssim$200 kyr) magnetic field. This is the first demonstration that some iron meteorites record ancient planetary magnetic fields. Furthermore, the observed field intensity, temporal variability and dynamo lifetime are consistent with thermal evolution models of the IVA parent core. Because the acquisition of remanent magnetisation by some IVA iron meteorites require that they cooled below their Curie temperature during the period of dynamo activity, the magnetisation carried by Steinbach also provides strong evidence favouring the inward solidification of its parent core.

1. Introduction

Collisions played a crucial role in the evolution of planetary bodies during the early history of the solar system. Depending on their relative sizes, velocities and trajectories, colliding bodies may have merged, been partially disrupted, or completely destroyed. A particular type of collision distinctive of the early solar system is hit-and-run collisions (Asphaug and Reufer, 2014), which involve two planetesimals colliding at a glancing angle. This impact is thought to be capable of stripping off part of the mantle of one body and either incorporating it into that of the other body or scattering it into space. Either way, models of this type of collision propose that it leaves behind a smaller, mantle-poor body, which, at its most extreme, may be just a naked molten core (Asphaug and Reufer, 2014). An extant asteroid that may be such a body is (16) Psyche, the only large (~100 km radius) body in the asteroid belt composed almost entirely of Fe–Ni metal (Matter et al., 2013). Without the insulation provided by overlaying silicate

* Corresponding author.
E-mail address: jfjb2@cam.ac.uk (J.F.J. Bryson).

http://dx.doi.org/10.1016/j.epsl.2017.05.026

material, a metallic asteroid is expected to have cooled far quicker than a mantled core and therefore may have solidified initially at its surface (Williams, 2009; Yang et al., 2007). As cooling continued, the solidification front could then have progressed towards the centre of the body, representing a solidification regime starkly different from the higher pressure, outwardly crystallising Earth's core.

There are several key unknowns regarding inward core solidification and its potential role in planetary magnetism. Firstly, although inward core solidification has been hypothesised for Mercury (Anderson et al., 2011), Ganymede (Hauck et al., 2006; Christensen, 2015; Ruckriemen et al., 2015), the Moon (Laneuville et al., 2014) and numerous asteroids (Williams, 2009), it is unknown whether this direction of core solidification actually occurs within planetary bodies because of uncertainties in the pressure derivative of the liquidus of low-pressure iron alloys. Secondly, even if inward core solidification does occur, it is unclear whether it could lead to dynamo activity (Nimmo, 2009). As a core outwardly solidifies (as for Earth), chemical segregation between the solid and liquid produces a gravitationally unstable density stratification in the liquid, causing it to convect and generate magnetic fields (Fearn and Loper, 1981). On the other hand, segregation during inward core solidification produces a gravitationally unstable solid and gravitationally stable liquid density stratification. Hence, if this process is capable of generating dynamo activity, it must be by a fundamentally different mechanism to that operating within Earth. Recently, several groups have conducted theoretical studies of dynamo generation during inward core crystallisation within Ganymede (Ruckriemen et al., 2015; Christensen, 2015; Hauck et al., 2006) and a mantle-stripped metallic asteroid (Scheinberg et al., 2016; Neufeld et al., in prep), proposing that magnetic fields could result from exotic, non-concentric solidification regimes such as Fe-snow or diapir dripping. Within a quickly cooling metallic asteroid, these mechanisms have been predicted to result in surface magnetic fields that decreased in intensity from ~200 μT down to 0 μT as the core solidified over a period of ~5–20 Myr, which could also have been quickly directionally varying (predicted local Rossby number significantly greater than 0.12, meaning variations were likely quicker than those of Earth's field; Olson and Christensen, 2006). Neufeld et al. (in prep) also propose that during the earliest stages of core solidification (first ~200 kyr), the thickness of the solid crust was too thin ($\lesssim$10 km) for it to delaminate so magnetic fields from diapir dripping are not expected during this very early period. By comparison, paleomagnetic studies of materials expected to originate from bodies that underwent inward core solidification have not been previously conducted. Here, we address this gap by presenting a paleomagnetic study of the IVA iron meteorites.

Very few previous paleomagnetic and rock magnetic studies have been conducted on iron meteorites due in part to their poorly understood remanence acquisition processes (Brecher and Albright, 1977; Funaki and Danon, 1998). Most fractionally crystallised iron meteorite families are thought to originate from mantled cores that cooled isothermally (Goldstein et al., 2009b), so would have been too hot (i.e., above the ordering temperature of their constituent Fe–Ni minerals) during the period of dynamo activity to have recorded the resulting fields (Cisowski, 1987). However, the IVA iron meteorites cooled faster (meteorites in this group have cooling rates ranging between ~10,000–100 °C/Myr at 500 °C; Yang et al., 2007) than most other iron meteorite families (typically <100 °C/Myr at 500 °C; Goldstein et al., 2009b) and their siderophile element trends suggest that the fastest cooled meteorites solidified first. These two observations indicate that the IVA meteorites originate from an unmantled core that inwardly solidified (Yang et al., 2007). Therefore, the surface of the IVA parent core could feasibly have been solid and below its magnetic ordering temperature while its interior was still molten, raising the possibility that the IVAs are a rare example of an iron meteorite family with the potential to have recorded planetary magnetic fields.

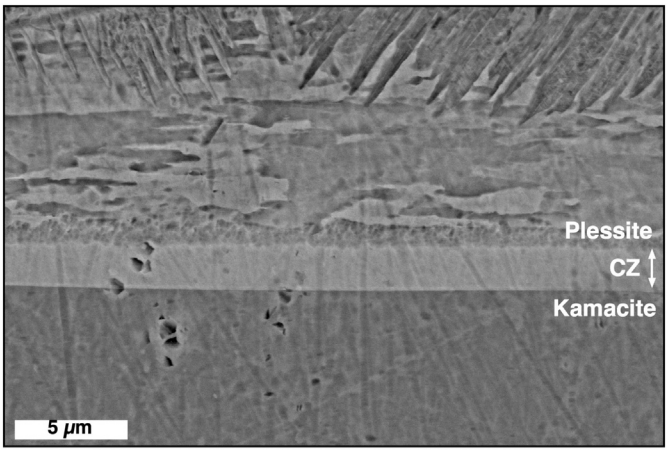

Fig. 1. Backscattered scanning electron microscope images of the microstructure in the Steinbach matrix metal along interface A. The kamacite, CZ and plessite are labelled.

A further complicating factor found by previous studies attempting to identify evidence of a natural remanent magnetisation (NRM) produced by ancient magnetic fields from iron meteorites is their poorly understood magnetic mineralogy (Brecher and Albright, 1977). However, recent advances in our understanding of the microstructure of iron meteorites and the Fe–Ni phase diagram combined with the development of microanalytical magnetic measurement techniques (Bryson et al., 2014b), now make paleomagnetic investigation of some iron meteorites feasible. The microstructure of the IVA iron meteorites formed via low temperature recrystallisation and consists of kamacite lamellae (Yang and Goldstein, 2005), adjacent to which are the tetrataenite rim (a ~0.2 μm rim composed of tetrataenite, chemically ordered $Fe_{0.5}Ni_{0.5}$), the cloudy zone (CZ, a nanoscale intergrowth of tetrataenite islands and an Fe-rich matrix, Goldstein et al., 2009b) and plessite (a μm-scale intergrowth of kamacite and tetrataenite laths) (Fig. 1). The relatively fast cooling rate of the IVA irons (Yang et al., 2007) means the length scales of all of these microstructures are smaller than those in most other irons (e.g., tetrataenite island diameters in the IVA meteorites are <30 nm, while they can be >100 nm in slower cooled meteorites; Goldstein et al., 2009b). Due to an underlying Ni concentration gradient, the formation age of the tetrataenite islands varies by millions of years across the width of CZ and, because the younger islands have had less time to coarsen, there is a corresponding decrease in island diameter across the CZ (Goldstein et al., 2009b; Bryson et al., 2014a). The kamacite lamellae, tetrataenite rim and plessite have all previously been shown to consist of numerous magnetic domains (Bryson et al., 2014b) and have relatively low coercivities of <10 mT, ~80 mT and 100–200 mT, respectively (Uehara et al., 2011; Gattacceca et al., 2014). Conversely, the small diameter of the tetrataenite islands means the CZ has a relatively high coercivity of 400–>1100 mT depending on distance across this intergrowth (Uehara et al., 2011). At the smallest diameters, the tetrataenite islands have been proposed to strongly interact magnetically, resulting in uniform magnetisation directions over thousands of neighbouring islands. These islands tend to display coercivities >1100 mT (Bryson et al., 2014a). The Steinbach and São João Nepomuceno (SJN) IVA iron meteorites also contain abundant silicate inclusions that contain Fe–Ni particles that can include CZ and plessite (Reisener and Goldstein, 2003).

A recent study has demonstrated that larger tetrataenite islands carry an extremely stable chemical transformation rema-

nent magnetisation (CTRM) (Bryson et al., 2014a). We have recently developed a technique that employs X-ray magnetic circular dichroism (XMCD), imaged using X-ray photoemission electron microscopy (XPEEM), to view the magnetisation of the CZ (Bryson et al., 2014b). This method can provide estimates of the intensity and direction of the ancient field experienced by the CZ and has previously been applied to main group pallasites (Bryson et al., 2015; Nichols et al., 2016).

We choose to measure the silicate inclusions extracted from the fastest cooled IVA meteorite, SJN (~10000 °C/Myr at 500 °C; Goldstein et al., 2009a; Yang et al., 2010), using superconducting moment magnetometry (Weiss and Tikoo, 2014), and the silicate inclusions and matrix metal of the slower cooled Steinbach meteorite (150 °C/Myr at 500 °C; Yang et al., 2007) using superconducting moment magnetometry and XPEEM, respectively. Both meteorites are largely unweathered finds and experienced shock pressures somewhere between 1–13 GPa (Goldstein et al., 2009a). We find that all our silicate subsamples from SJN and some silicate subsamples from Steinbach are poor magnetic recorders and do not contain robust records of ancient magnetic fields, introducing the possibility that either a remanence was never imparted to these components or a remanence has been lost due to viscous decay or shock remagnetisation (Goldstein et al., 2009a; Tikoo et al., 2015). On the other hand, the matrix metal and other silicate subsamples in Steinbach display better recording potential. Most importantly, XPEEM measurements of the matrix metal in this meteorite provide evidence of intense and directionally varying fields on the IVA parent body, consistent with predictions from recent modelling studies that dynamo activity can be driven by exotic, non-concentric inward crystallisation regimes (Scheinberg et al., 2016; Neufeld et al., in prep). The existence of this remanence supports the proposed origin of the IVA meteorites from an unmantled and inwardly solidifying core, demonstrates that inward core solidification is capable of generating dynamo activity, and establishes that iron some meteorites can provide interpretable paleomagnetic records.

2. Samples and methods

2.1. Silicate demagnetisation measurements

The silicate inclusions in Steinbach and SJN consist predominantly of pyroxene and are thought to represent a residuum of silicate material that remained on the IVA parent core after its mantle was removed (Ruzicka and Hutson, 2006; Wasson et al., 2006). We extracted mutually oriented, mm-sized subsamples of silicates from slabs of Steinbach and SJN provided by the United States National Museum of Natural History (USNM, sample numbers USNM5298 and USNM6881, respectively) using a wire saw (Figs. S1, S2). Our slab of SJN contained fusion crust along one edge and we cut subsamples from two assemblages that were >10 mm from the fusion crust and one that was 4 mm from the fusion crust. Our slab of Steinbach did not contain fusion crust.

Alternating field (AF) demagnetisation of these silicates was performed using a 2G Enterprises Superconducting Rock Magnetometer 755 housed in a shielded room (DC field <200 nT) in the Massachusetts Institute of Technology (MIT) Paleomagnetism Laboratory. Both Steinbach and SJN silicate subsamples were AF demagnetised using an automated three-axis procedure up to 145 mT. The AF was applied along each orthogonal axis and the sample moment measured after each AF application. All measurements for each AF intensity were averaged following the Zijderveld–Dunlop protocol to mitigate the effects of spurious anhysteretic remanent magnetisation (ARM) and gyroremanent magnetisation (GRM) (Stephenson, 1993). One Steinbach subsample (STB-5g) was additionally AF demagnetised in this manner up to 420 mT, the maximum field intensity reachable with our AF coil, and then subjected to further three-axis DC demagnetisation up to 1100 mT by applying oppositely oriented isothermal remanent magnetisations (IRMs) in steps of 0.1 T. NRM components were identified using principal component analysis (Kirschvink, 1980).

Following NRM demagnetisation, we applied and demagnetised ARMs (AC fields of 260 mT and DC fields of 50 μT) and IRMs (260 mT) to the subsamples to constrain the intensity of the fields that imparted the NRMs (Weiss and Tikoo, 2014). We choose to adopt non-heating methods because tetrataenite disorders at 320 °C (Yang et al., 1996), which would invalidate paleointensity estimates from such methods. Paleointensities from the ARM (P_{ARM}) and IRM (P_{IRM}) methods were calculated as:

$$P_{ARM} = \frac{\Delta NRM}{\Delta ARM}\frac{b}{f'} \quad (1)$$

$$P_{IRM} = \frac{\Delta NRM}{\Delta IRM}a \quad (2)$$

where ΔNRM, ΔARM and ΔIRM are the changes in NRM, ARM and IRM during demagnetisation, respectively, b is the DC bias field, f' is the ratio of the thermoremanent magnetisation (TRM) to the ARM and a is constant with units of field that depends on the IRM/TRM ratio (Tikoo et al., 2014). We adopted values of $f' = 1.34$ for $a = 3000$ μT, which have been previously calibrated for TRMs carried by kamacite-bearing samples (Tikoo et al., 2014; Weiss and Tikoo, 2014; Lappe et al., 2013). Although the IVA meteorites contain a variety of magnetic minerals other than kamacite (including taenite, martensite and tetrataenite), the values of f' and a for these minerals are unknown, so we chose to adopt the above values for all the phases present in these samples. The contributions from taenite and martensite to the total magnetisation of these subsamples are difficult to estimate as the magnetic properties of these phases are expected to be similar to those of kamacite, so they cannot be readily isolated from our magnetic measurements. However, this expected similarity also means that the values of f' and a for these phases are likely similar to those we adopt for kamacite. We suspect that the contribution from single domain tetrataenite dominates at AF intensities >145 mT as there are few other magnetic carriers in these samples expected to have such high coercivities. Also, previous studies suggest CTRMs can be a factor of 1–10 times weaker than TRMs acquired in the same paleofield (McClelland, 1996; Smirnov and Tarduno, 2005), suggesting that the paleointensity estimates we present from CTRMs (calculated using the TRM-calibrated f' and a values) are lower bounds. These effects, coupled with the estimated 2σ uncertainties of a factor of 5 for the values of f' and a, are the dominant source of error in our estimates (Weiss and Tikoo, 2014). Our stated errors are 95% confidence values that are calculated during the formal slope-fitting procedure.

Following Tikoo et al. (2014), we also constrained the paleomagnetic fidelity of our subsamples by measuring the minimum field intensity that we could reliably recover using our instrumentation. This was achieved by applying and demagnetising laboratory ARMs imparted with DC bias fields of 50 μT, 100 μT and 150 μT (AC field of 260 mT) and attempting to retrieve these bias field values by normalisation to a 300 μT bias field ARM. Tikoo et al. (2012) present difference (D) and error (E) metrics:

$$D = \frac{|L - I|}{L} \quad (3)$$

$$E = \frac{W}{L} \quad (4)$$

where L is the applied laboratory intensity, I is the retrieved intensity and W is the 95% confidence on the retrieved intensity. Tikoo et al. (2012) suggest that a value >1 in either metric corresponds to a poor recorder. However, we note that any value of I

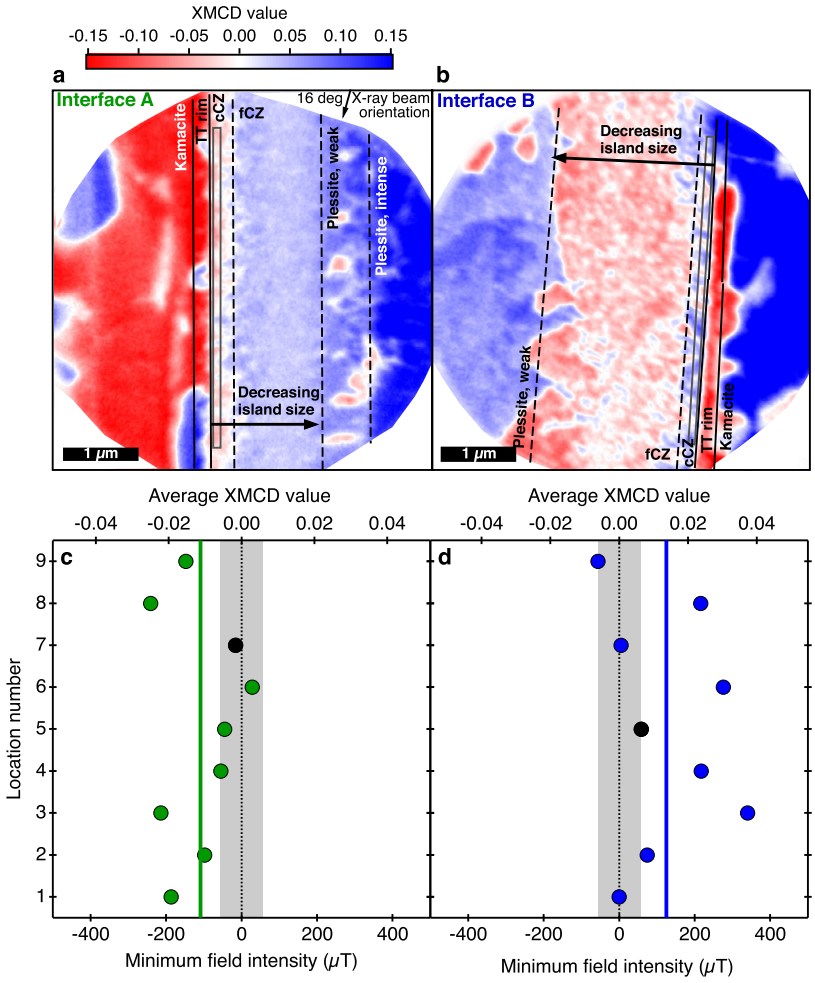

Fig. 2. X-ray photoemission electron microscopy (XPEEM) images of the CZ in the Steinbach meteorite. Representative XPEEM images from a) interface A and b) interface B. The kamacite, tetrataenite (TT) rim, coarse CZ (cCZ), fine CZ (fCZ) and plessite regions with different XMCD intensities (plessite, weak and plessite, intense) are labelled. The chemical boundaries between the kamacite, tetrataenite rim and CZ are marked with solid lines and the changes in magnetic behaviour between the coarse and fine CZ and plessite regions are marked with dashed lines. Positive (blue) and negative (red) XMCD intensities correspond to positive and negative projections along the X-ray beam direction. c), d) Average XMCD intensity extracted from the coarse CZ (represented by the grey boxes in a) and b)) and the recovered minimum paleointensity from each location imaged along interface A and B, respectively. The average of the average XMCD values along each interface are displayed as the bold coloured lines. The black points in c) and d) are the average XMCD values extracted from a) and b), respectively. Positive and negative minimum field intensities correspond to fields with the same intensity but different projections onto the X-ray beam direction. The grey shaded regions correspond to the 2σ of the distribution of average XMCD values expected for CZ formation in the absence of a field (see Supplementary Material). (For interpretation of the references to colour in this figure legend, the reader is referred to the web version of this article.)

between 0 and L will produce a D value <1, which would classify the subsample as a good recorder even if I is tens or hundreds of μT below L. We therefore propose a new metric D':

$$D' = \frac{I - L}{L} \tag{5}$$

A positive critical value of 1 still exists for D', but we now also propose a negative critical value of -0.5. These critical values correspond to a factor of 2 greater and less than the laboratory field, respectively. Adopting D' also means the critical value of E should be updated to 0.5 as the value of W that produces $D' < -0.5$ is reduced by a factor of 2 compared to that in Tikoo et al. (2012).

2.2. X-ray microscopy

XPEEM images of the CZ in Steinbach (largest CZ island diameter of 29 nm; Goldstein et al., 2009a) were performed on pure matrix metal samples provided by the Natural History Museum, London (sample number BM.35540) at the UE49 end station, at the Berliner Elektronenspeicherring-Gesellschaft für Synchrotronstrahlung (BESSY) II synchrotron. To infer the ancient field properties from XPEEM images, we calculated the average XMCD value within a 100-nm × ~4000-nm region among the coarsest islands in each image captured (grey boxes Fig. 2a, b). The ancient field properties were then calculated by comparing these average XMCD values to those predicted for a range of paleofield intensities and directions (see Supplementary Material). Because we only measure the projection of the local magnetic moment onto one orientation of the X-ray beam, we can only constrain the magnetisation direction to within a hemisphere centred on the X-ray beam direction. Therefore, we also cannot uniquely constrain the paleointensity but only determine its minimum value. Furthermore, due to uncertainties in the growth rate of the islands, we assume that the blocking volume of the islands is the same as their present day volume (see Supplementary Material). The islands will have been smaller than this size when they recorded a field, meaning that they will have had a smaller moment than the value we adopted and had to experience a stronger paleointensity than the value we present to generate the observed XMCD values. Hence, the values we present are extreme lower limits on the paleointensity.

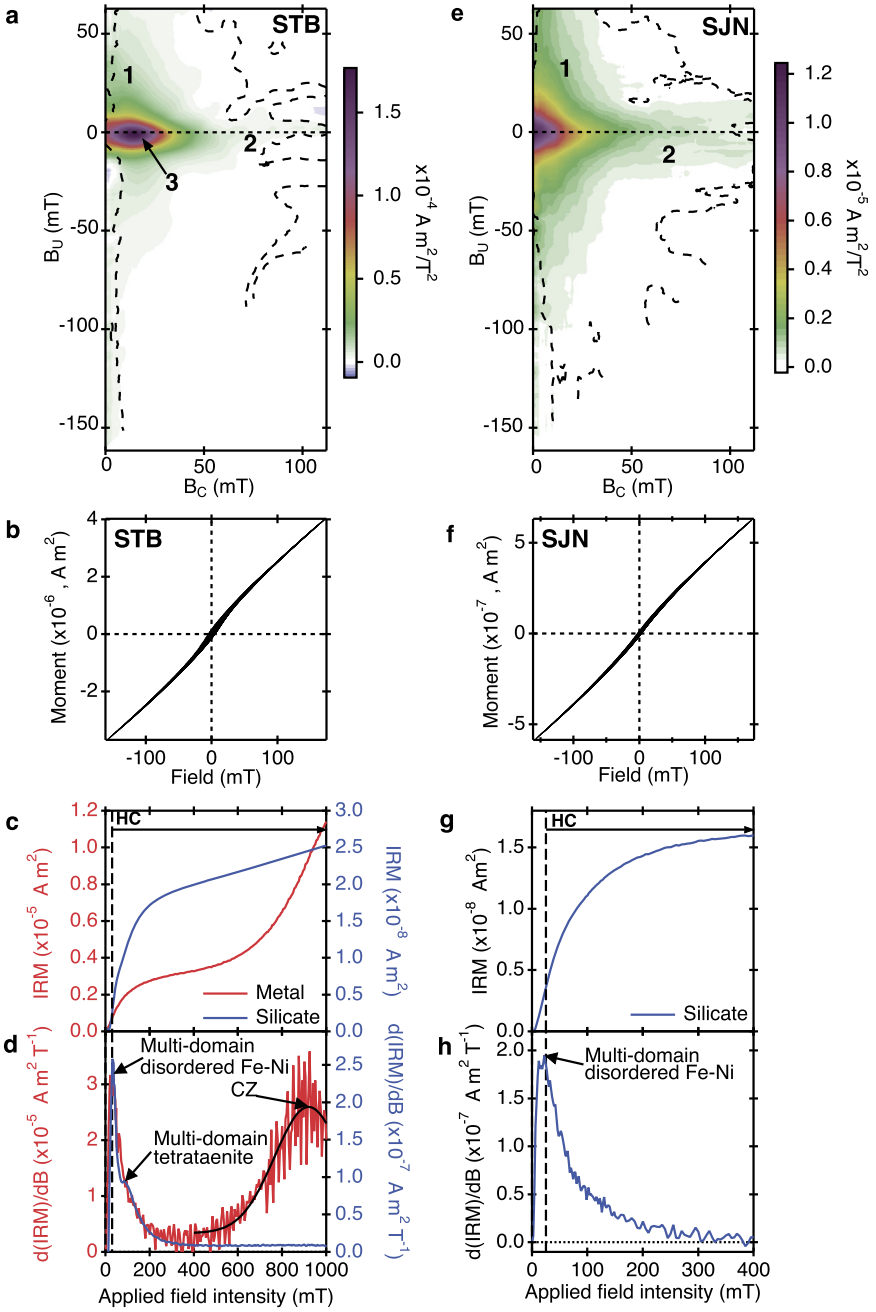

Fig. 3. a), b) FORC diagram and FORCs, respectively, for Steinbach silicate subsample STB-1c. The colour of the FORC diagram depicts the proportion of particles with a given coercivity, B_c, that experience a given interaction field, B_u. The numeric labels indicate the components of the signal that correspond to different families of magnetic particles discussed in Section 3.1.1. The hysteresis loop is uncorrected for paramagnetic effects and is slightly open at weak field values. c), d) IRM acquisition and corresponding coercivity spectra for silicate subsample STB-5d (blue) and matrix metal subsample STB-M (red). The magnetic carriers relating to the different peaks are labelled. The coercivity spectrum of the matrix metal subsample displays a clear peak centred at 900 mT (Gaussian curve fit included in black to depict the shape of the curve), corresponding to coarse CZ islands, that is absent from the silicate subsample. The HC magnetisation range extends from a minimum field of ~25 mT (vertical dashed line) to beyond 1000 mT. e), f) FORC diagrams and FORCS, respectively, for SJN silicate subsample SJN-8c. The hysteresis loop is slightly less open at weaker field values than that of Steinbach. g), h) IRM acquisition and corresponding coercivity spectra for SJN silicate subsample SJN-8c. (For interpretation of the references to colour in this figure legend, the reader is referred to the web version of this article.)

3. Results

3.1. Steinbach

3.1.1. Magnetic domain state of matrix metal and Steinbach silicates

Hysteresis properties and first order reversal curves (FORCs) (Harrison and Feinberg, 2008) were measured on one Steinbach silicate subsample (STB-6) (Fig. 3a, b). The ratios of saturation remanent magnetisation (M_{rs}) to saturation magnetisation (M_s) of 0.023 and the coercivity of remanence (B_{cr}) to the coercivity (B_c) of 3.74 imply that this subsample likely contains predominantly low coercivity multi-domain (MD) and coarse pseudo single-domain (PSD) Fe–Ni particles. The FORC diagrams from both Steinbach and SJN (Section 3.2.1) are composed of varying contributions of three separate components: the first component is a clear MD signal at low coercivity signal (up to ~20 mT); the second is a weaker higher coercivity signal (up to 80–100 mT) that is spread in values of interaction fields, B_u; the third is a clear interacting single domain (SD) or PSD signal with a peak at ~15 mT

and extending only as far as 60–80 mT. The components most likely originate from large kamacite grains, laths in the plessite, and small kamacite or martensite grains that form through low temperature recrystallisation, respectively. The Steinbach subsample contains all three of these components. Although the coercivity of the third component only extends up to 60–80 mT, these particles have the potential to be reliable magnetic recorders, introducing the possibility that some Steinbach silicate subsamples may provide reliable paleomagnetic data.

The coercivity spectrum of one matrix metal (STB-M) and one silicate (STB-5d) Steinbach subsample (Figs. 3c, d) were also characterised by imparting incrementally stronger IRMs up to 1000 mT to the subsamples. The coercivity spectrum of the matrix metal displays a narrow peak at ∼25 mT that likely corresponds to MD and PSD kamacite and martensite and a shoulder peak at 85 mT that has previously been ascribed to MD tetrataenite (Gattacceca et al., 2014). There is also a broad peak centred at ∼900 mT that should correspond to the CZ (Gattacceca et al., 2014; Uehara et al., 2011). The coercivity spectrum of the silicate subsample shows the same low coercivity peak as the matrix metal subsample, implying the presence of MD kamacite and martensite, and displays a constant, low value at intensities >400 mT, implying the presence of tetrataenite but in lower relative abundance than the matrix metal.

3.1.2. XPEEM observations of matrix metal in Steinbach

The CZ magnetisation was measured systematically at nine locations along the length of two interfaces in the Steinbach sample (interfaces A and B, Fig. S4). Representative XPEEM images from each interface are shown in Fig. 2a, b (additional images are included in Figs. S5 and S6). Positive and negative projections of the local magnetic moment onto the X-ray beam direction correspond to blue and red signals, respectively. The kamacite consists of a few large (∼1–5 μm) magnetic domains. The tetrataenite rim consists of more, smaller ($\lesssim$2 μm) domains. The entire CZ is ∼1–2 μm wide along both interfaces and its signal varies between the interfaces. The signal in the coarse CZ (immediately adjacent to the tetrataenite rim containing islands ∼29–20 nm in diameter) is similar to that observed in previous XPEEM studies (resembles a collection of nm-scale, independently magnetised islands; Bryson et al., 2014b) and is thought to contain non-interacting tetrataenite islands that have previously provided reliable paleomagnetic information (Bryson et al., 2015; Nichols et al., 2016). The magnetisation of fine CZ (further from the tetrataenite rim containing islands $\lesssim$20 nm diameter) is thought to be dominated by interactions between neighbouring tetrataenite islands that produce uniform magnetisation direction over μm length scales (Bryson et al., 2014a, 2014b). The magnetic signal of the plessite consists of an initial region adjacent to the fine CZ that consists of a relatively weak XMCD signal ('plessite, weak' in Figs. 2a, b) and a second region (∼4 μm from the tetrataenite rim) consists of a more intense XMCD signal ('plessite, intense').

3.1.3. Ancient field properties from XPEEM of matrix metal in Steinbach

The minimum intensity and polarity of the field experienced by Steinbach were calculated from the average XMCD values extracted from the coarse CZ in each image along both interfaces (Fig. 2c, d). We restricted our region of interest to the coarse CZ as the signal in this region does not appear to be influenced by magnetic interactions between islands. This region is ∼100 nm wide, which is far narrower than that observed in previous studies (Bryson et al., 2015; Nichols et al., 2016) due to the relatively steep bulk Ni gradient across the CZ resulting from the fast cooling rate of the IVA iron meteorites. The average XMCD values along interface A and B have similar magnitudes and mostly opposite signs. Calculating paleointensities from these signals produces minimum values ranging between 0 and 300 μT for the different locations (see Supplementary Material) and average minimum paleointensities along interface A and B of 110 μT and 125 μT, respectively. The change in sign means the calculated range of possible field directions from each interface are non-overlapping, suggesting that the fields that magnetised these interfaces were differently oriented.

3.1.4. Moment magnetometry of Steinbach silicates

AF demagnetisation of silicates extracted from our Steinbach slab identified a low-coercivity (LC, typically 0–∼25 mT) component that is similarly oriented among all eight subsamples (Figs. 4a, b, c). At high coercivities (HC, ∼25–145 mT), none of the subsamples contained a clear NRM component, although most subsamples experienced weak, non-origin-trending (mean angular deviation [MAD] less than the deviation angle [DANG]; Tauxe and Staudigel, 2004) and non-unidirectional changes in magnetisation (Fig. 4d, Table S1). These subsamples did not experience significant demagnetisation even by 145 mT, with an average of 81% of the NRM remaining at this AF intensity. Subsample STB-5g did not experience significant demagnetisation even after DC demagnetisation up to 1.1 T (green points Fig. 4b). The directions of the remanence remaining after an AF intensity of 145 mT are non-unidirectional (Fig. 4e). Such hard magnetisation must correspond to tetrataenite within the CZ because no other phases present have such high coercivity (Fig. 3d) (Bryson et al., 2014b, 2014a; Uehara et al., 2011).

3.1.5. Paleointensities of Steinbach silicates

We obtained estimates of the intensity of the field that imparted the NRM to the Steinbach silicates by comparing AF demagnetisation of the NRM with that of an ARM (peak AC field 260 mT, DC bias field 50 μT) and/or a saturating IRM (Tikoo et al., 2014). These values are somewhat uncertain as the remanence in Steinbach is carried by a range of magnetic phases and is likely in the form of a CTRM acquired during low temperature recrystallisation, meaning our paleointensity estimates are likely a factor of 1–10 times weaker than the actual ancient field intensities (McClelland, 1996; Smirnov and Tarduno, 2005). The average LC paleointensities calculated from the ARM and IRM methods are 47 ± 12 μT and 17 ± 4 μT (2σ, average of 4 and 6 subsamples), respectively (Figs. 4f, S3a). The HC magnetisations, which are an average of two orders of magnitude above the 10^{-12} A m^2 noise limit of our magnetometer (Wang et al., 2017), correspond to average paleointensities within error of zero: 0 ± 5 μT and −1 ± 3 μT for the ARM and IRM methods (2σ, average of 4 and 6 subsamples), respectively (Fig. 4f). Combined with the non-unidirectional and non-origin-trending nature of the HC magnetisation, these paleointensities indicate that no NRM is blocked in the HC range.

This observation suggests that the average field experienced by these subsamples may have been too weak to impart a reliable HC remanence to these subsamples. Our paleointensity fidelity measurements for STB-8c produce values of D' between −0.5 and 1 and values of E that are all less than 0.5 in both coercivity ranges, implying that this subsample is capable of reliably acquiring a thermoremanence in the presence of field intensities as weak as a few tens of μT (Fig. 5a). Accounting for the uncertainties in recording efficiency of a CTRM, this recording limit could increase to a few hundred μT for chemical remanences. On the other hand, the HC values of E for STB-3b are greater 0.5 for a 37 μT and 75 μT field and the HC values of D' for fields of 75 μT and 112 μT are greater than 0.5 (Fig. 5b). Together, these observations imply that STB-3b is a far poorer recorder than STB-8c, probably requiring field intensities $\gtrsim$100 μT to reliably impart a HC thermoremanence and possibly up to 1000 μT for a chemical remanence. Different Steinbach subsamples therefore appear to have different paleomagnetic fidelities.

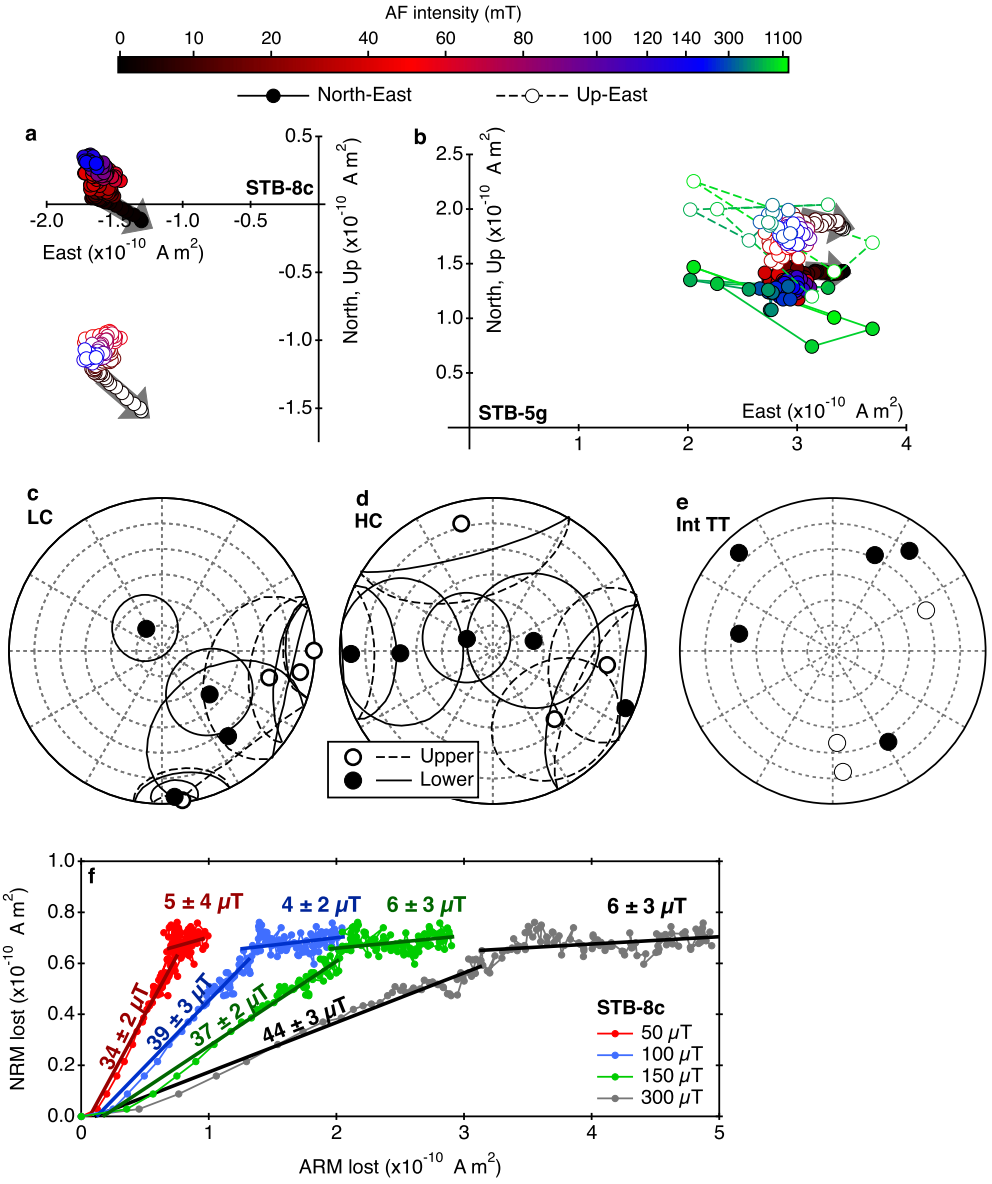

Fig. 4. AF demagnetisation of NRM in Steinbach silicates. Orthographic projection plots showing AF demagnetisation of a) STB-8c and b) STB-5g. Open and closed points represent projections of the end point of the NRM vector onto the horizontal (north-east) and vertical (up-east) planes, respectively. The colour of each point represents the AF intensity according to the colour scale. Grey arrows denote the directions of LC components. c), d), e) Equal area stereoplots showing the directions of the LC component, HC magnetisation and the NRM vector after an AF intensity of 145 mT, respectively. The directions in e) correspond to the net magnetisation direction of the interacting tetrataenite (int TT). Open points and dashed lines correspond to the upper hemisphere of the stereoplot and closed points and solid lines correspond to the lower hemisphere. Maximum angular deviation (MAD) angles are included around each point in c) and d). f) Paleointensity calculation using the ARM method for STB-8c. The two values for each ARM curve represent the paleointensities of the LC and HC components. (For interpretation of the references to colour in this figure legend, the reader is referred to the web version of this article.)

3.2. SJN

3.2.1. Magnetic domain state of SJN silicates

We measured hysteresis curves and FORC diagrams of one silicate subsample (SJN-8c) extracted from our slab of SJN (Fig. 3e, f). Similar to the Steinbach silicate, the M_{rs}/M_s value of 0.034 and B_{cr}/B_c value of 6.14 suggest that the ferromagnetic grains in SJN are predominantly MD and coarse PSD, and are therefore likely poor paleomagnetic recorders. The FORC diagram only contains the first and second components discussed in Section 3.1.1, suggesting the carries in this subsample are interacting MD kamacite and plessite.

Similar to Steinbach, the coercivity spectrum of SJN silicates (Figs. 3g, h) contains a peak at ~25 mT that likely corresponds to MD and coarse PSD kamacite. However, unlike Steinbach, the SJN subsample appears to saturate by 400 mT, suggesting the absence of tetrataenite in this meteorite. This is most likely due to the inhibition of some low temperature phase transitions due to the fast cooling rate of this meteorite. This observation also suggests that other low temperature transformations such as kamacite nucleation and martensite decomposition could be incomplete, introducing the possibility that SJN carries a combination of a TRM and a CTRM. The paleointensity estimates from this meteorite will therefore suffer from the same uncertainties as Steinbach, possibly being a factor of 1–10 times less than the actual ancient field intensities.

3.2.2. Moment magnetometry of SJN silicates

Four and seven subsamples were taken from silicate assemblages located at distances of 4 mm and >10 mm from the exterior of our SJN slab, respectively. Unlike Steinbach, all of the

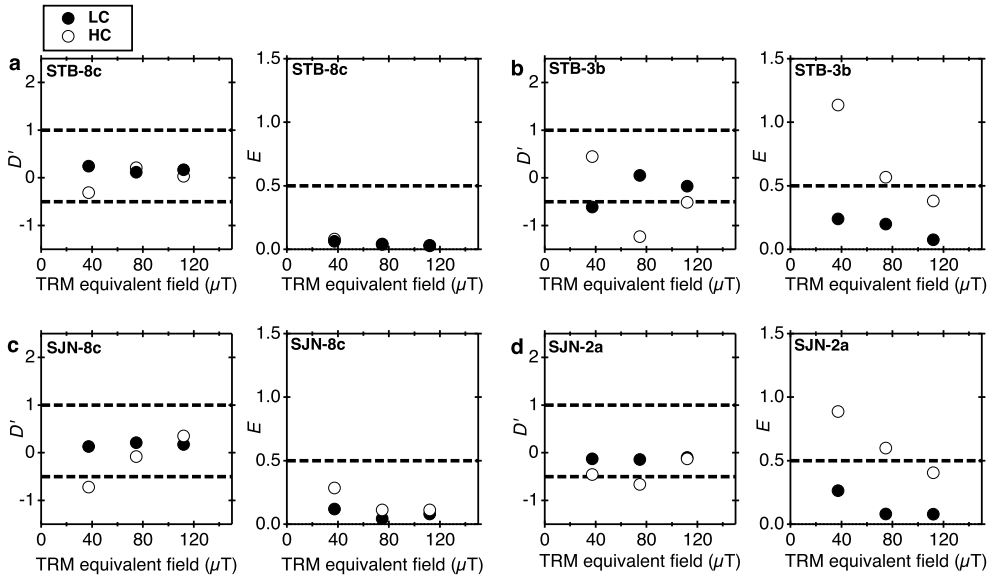

Fig. 5. D' and E values for silicate subsamples a) STB-8c, b) STB-3b, c) SJN-8c and d) SJN-2a. The LC and HC components are shown as filled and open points, respectively. Any D' data points greater than 1 or less than −0.5 (i.e., above the top dashed line or below the bottom dashed line) or E values greater than 1 (i.e., above the dashed line) correspond to poor paleomagnetic fidelities, which is the case for some applied ARMs in HC range in STB-3b, SJN-8C SJN-2a, as well as the LC range in STB-3b.

directionally stable NRM in our SJN subsamples was demagnetised by an AF intensity of only 20–50 mT (Figs. 6a, b), reaffirming the absence of tetrataenite and the poor paleomagnetic fidelity of the silicates from this meteorite. All subsamples contain an LC component (0–∼20 mT) and one subsample may also contain a medium coercivity (MC) component (∼20–∼50 mT, red arrows, Fig. 6b). None of the subsamples contain an HC component (∼20–145 mT, purple and blue points, Figs. 6a, b, d) even though IRM acquisition measurements demonstrate that there are significant quantities of grains in this coercivity range (Fig. 3g). The intensities of the LC components in subsamples from within 4 mm of the sample surface are typically an order of magnitude stronger than those from the sample interior. Furthermore, the directions of the LC component from the subsamples within 4 mm of the fusion crust are mostly unidirectional and origin-trending, while those from the interior are non-unidirectional and mostly non-origin-trending (Fig. 6c, Table S2). These observations correspond to a positive baked contact test, demonstrating that the NRM of the interior subsamples is pre-terrestrial.

3.2.3. Paleointensity of SJN silicates

The ARM and IRM methods yield average LC paleointensities from subsamples 4 mm from the exterior of the meteorite of 121 ± 31 μT and 116 ± 10 μT (2σ), respectively, while interior subsamples yield average values of 34 ± 20 μT and 63 ± 27 μT, respectively. Subsamples within 4 mm of the sample surface yield average HC paleointensities of -3 ± 6 μT and 26 ± 16 μT, respectively, while interior subsamples yield average paleointensities of 2 ± 8 μT and -2 ± 44 μT, respectively (Fig. 6e).

Again, the weak HC paleointensities could reflect the poor paleomagnetic fidelity of SJN silicates in the HC range (Figs. 5c, d). For SJN-8c and SJN-2a, the values of D' in the HC range are less than −0.5 for thermal field intensities of 37 μT and 75 μT, respectively. For SJN-2a, the HC values of E are also greater than 0.5 for thermal field intensities of 37 μT and 75 μT. These observations suggest that SJN silicates are poor recorders, likely also requiring fields $\gtrsim$100 μT to impart a reliable HC TRM and possibly up to 1000 μT to impart a reliable HC CTRM.

4. Discussion

4.1. Ancient field properties from XPEEM of Steinbach

The sign of the average XMCD values extracted from the coarse, non-interacting CZ in the XPEEM images differ between interface A and B, while the absolute values of these XMCD signals and the calculated minimum paleointensities of >109 μT and >125 μT are similar. We propose two likely explanations for these observations:

1. The CZ along interfaces A and B formed at different times, between which the field orientation varied but the intensity remained approximately constant.
2. The two signals are the result of statistical fluctuations possible for a small number of magnetic carriers that formed in zero field (Berndt et al., 2016).

To assess whether our measured signals are consistent with zero field magnetisation, first we calculated the average XMCD value we would expect if the ∼140 islands in each of our regions of interest formed in the absence of a field (see Supplementary Material). We repeated this process 9 times (reflecting the number of images we captured along each interface), calculating an average XMCD value equivalent to the value we measured along each interface. We repeated this process 10,000 times to produce the distribution of simulated average XMCD values we would expect in the absence of a field. Twice the value of the standard deviation of this distribution is included in Figs. 2c, d as the grey bars, which indicate the 95% confidence intervals that a measured XMCD signal could have been generated in the absence of a field. Although some of the individual measured average XMCD values lie within these ranges, the average measured value along each interface does not, suggesting that the NRM does not correspond to zero field magnetisation. This conclusion was reached by comparing the same number of measured and simulated islands, allowing us to conclude that, although we studied a small number of magnetic carriers, we are confident that our signal is inconsistent with the absence of a field. Moreover, a Student's t-test demonstrates that the chance that the mean of average XMCD values along interface A and B is zero at the 95% confidence level is 0.8% and

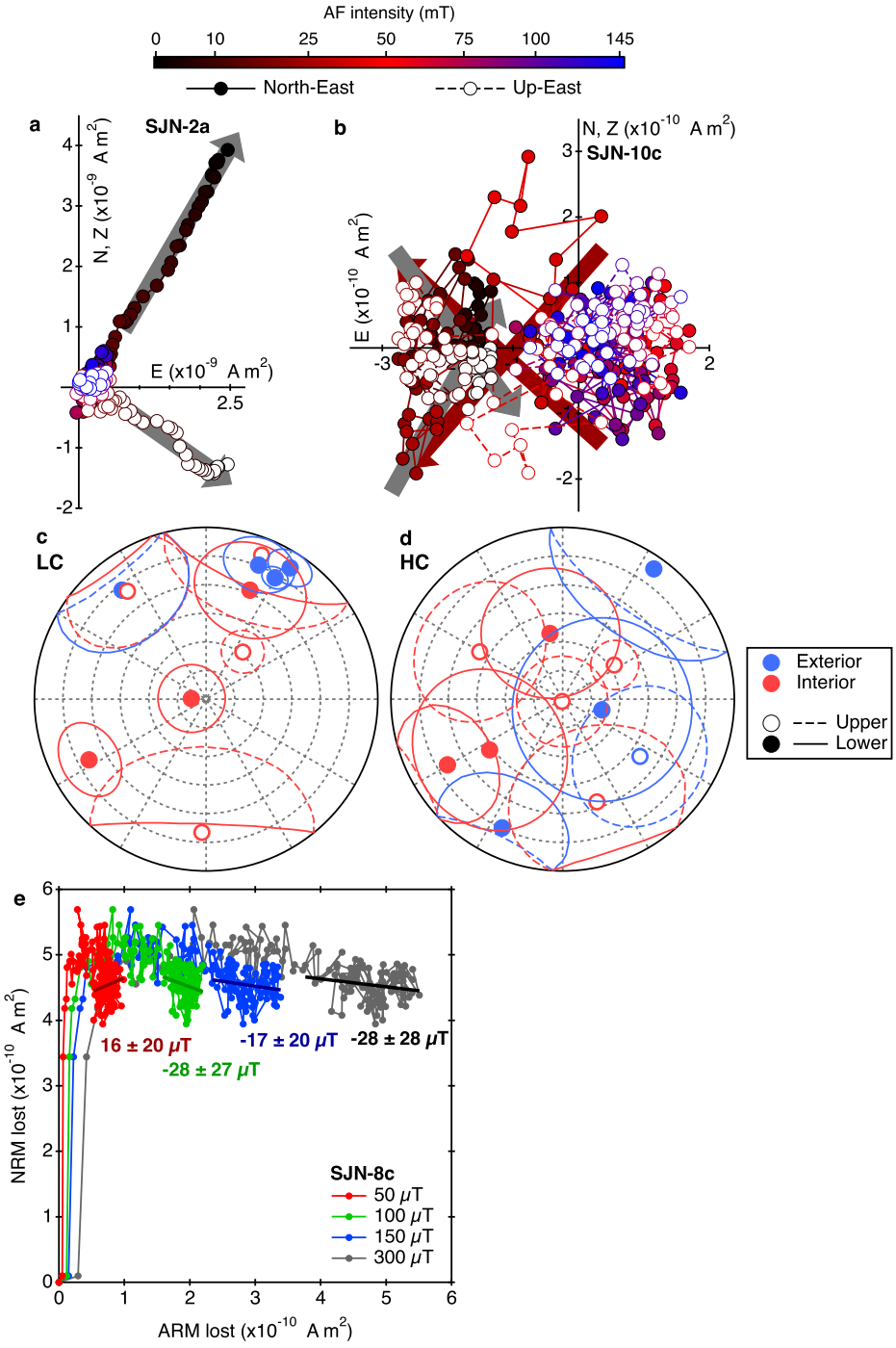

Fig. 6. AF demagnetisation of SJN silicates. Orthographic projection plot of the AF demagnetisation of a) SJN-2a and b) SJN-10c. Open and closed points represent projections of the endpoint of the NRM vector onto the horizontal (north-east) and vertical (up-east) planes, respectively. The colour of the point represents the AF intensity, according to the colour scale. Grey and crimson arrows denote the directions of LC and MC components, respectively. Equal area stereoplots showing the direction of the c) LC and d) HC components, respectively. Blue and red points correspond to samples 4 mm and >10 mm from the sample exterior, respectively. Open points and dashed lines correspond to the upper hemisphere of the stereoplot and closed points and solid lines correspond to the lower hemisphere. MAD angles are included as rings around each point in c) and d). e) Paleointensity calculation from the ARM method for SJN-8c. The values for each ARM curve correspond to the paleointensity of the HC range. (For interpretation of the references to colour in this figure legend, the reader is referred to the web version of this article.)

2.7%, respectively (Weisberg, 1985). Our data therefore suggest that the IVA parent core generated a directionally varying field, which would require that interface A and B recorded their NRMs at different times during planetary cooling. The Fe–Ni phase diagram (Uehara et al., 2011) demonstrates that the CZ formation temperature (and hence formation time) depends on the local Ni concentration, so we expect that the Ni concentrations along these interfaces must differ. Using XPEEM, we measured the Ni/Fe ratio at one location along interfaces A and B and found that the Ni concentration is ∼1.5% greater among coarse islands along interface A than interface B (Fig. 7). At the cooling rate of the Steinbach meteorite (∼150 °C/Myr at 500 °C; Yang et al., 2007), this compositional difference corresponds to a ∼200 kyr difference between CZ formation along these interfaces (see Supplementary Material). It is therefore feasible that the interfaces their NRMs at different times during planetary cooling. Our observations therefore imply

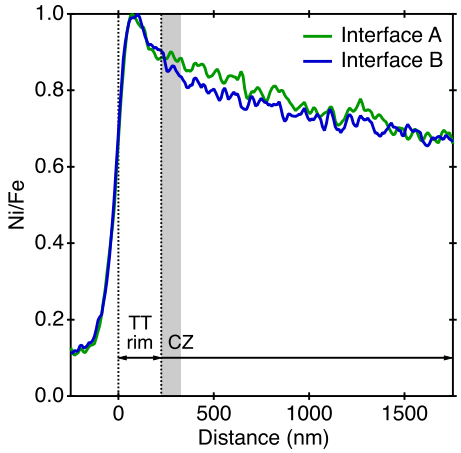

Fig. 7. Ni/Fe ratio across the CZ at one location along interfaces A (green) and B (blue) measured using XPEEM. The location of the coarse CZ is depicted by the grey bar and contains a ∼1.5% higher Ni concentration along interface A than interface B. (For interpretation of the references to colour in this figure legend, the reader is referred to the web version of this article.)

that the field generated by the IVA parent core changed orientation on a timescale <200 kyr and was ≳100 μT.

This observation implies that Steinbach must have been below its magnetic ordering temperature while a dynamo was active, supporting the unmantled structure and inward solidification of the IVA parent core. Furthermore, this observation demonstrates that inward core solidification is capable of generating a dynamo, and the observed properties are consistent with the ≲200 μT intensity and quickly directionally varying field predicted by recent models of non-concentric core solidification (Scheinberg et al., 2016; Neufeld et al., in prep).

4.2. Moment magnetometry of silicates from Steinbach

Although the unidirectional LC remanence observed during silicate demagnetisation is consistent with Steinbach having experienced a unidirectional field on the parent body, the ease with which the MD grains that carry this remanence can be remagnetised by weak shock events (<2 GPa; Tikoo et al., 2015) or overprinted by viscous remanent remagnetisation acquired in the geomagnetic field means this remanence may not be extraterrestrial. Given the Earth-like recovered paleointensities of 47 ± 12 μT and 17 ± 4 μT for the ARM and IRM methods, respectively, in this coercivity range, we propose this remanence likely reflects viscous remagnetisation after the meteorite landed on Earth.

We found that the Steinbach silicates do not contain a HC remanence and that the ability of these grains to acquire such a remanence varied among subsamples. Importantly, some subsamples are capable of acquiring a reliable HC remanence from fields with intensities between several tens to hundreds of μT. These values range from weaker than to comparable to the intensity inferred from our XPEEM measurements (≳100 μT, Section 3.1.3), so we may expect these subsamples to carry a reliable remanence. However, these XPEEM measurements also suggest that the field orientation varied on a timescale <200 kyr. Coupled with Steinbach's slow cooling rate (150 °C/Myr; Yang et al., 2007), we expect that the orientation of the field experienced by this meteorite during the period the HC component was recorded likely varied significantly >10 times. The HC magnetisation is therefore the average of a relatively quickly changing field, which we expect would result in the non-unidirectional remanence, absence of a clear loss of HC magnetisation and the weak paleointensities we observe in AF demagnetisation as well as the CZ signal we observe in XPEEM.

It is also possible that, given the upper limit on the fidelity of some of these subsamples (possibly requiring field intensities up to 1000 μT to acquire a HC remanence), these subsamples experienced too weak a field for a HC remanence to be imparted. In this case, it is worth noting that at the time of tetrataenite formation, the metal surrounding the silicates consisted of magnetically soft kamacite and taenite (Yang and Goldstein, 2005). The high magnetic permeability of these phases (Bryson et al., 2015) allows them to redirect an external field around the inclusions, acting to amplify the intensity of the field within the metal (see Supplementary Material) and reduce the intensity of the field that penetrates into the silicates. The extent of this shielding is poorly understood, but has been proposed to reduce the field intensity within the silicates by a factor of >2 compared to that of the external field (Bryson et al., 2015; Tarduno et al., 2012). Different models of dynamo generation on the IVA parent body (Scheinberg et al., 2016; Neufeld et al., in prep) predict that it could have generated field intensities ≲200 μT when Steinbach would have cooled through its magnetic ordering temperature, so we anticipate the intensity of the field within the silicates could be <100 μT, which was probably too weak to impart a reliable remanence to the silicates with poorer paleomagnetic fidelities.

The direction of the moments remaining after AF demagnetisation up to 145 mT are non-unidirectional among the Steinbach subsamples (Fig. 4e). The majority of this signal originates from the remanence carried by the CZ. The magnetisation of the fine CZ islands is particularly poorly understood, although it is clear that the magnetisation of this region is influenced by magnetic interactions, which likely reduces the ability of these islands to record a reliable remanence (Bryson et al., 2014b, 2014a). The XPEEM results demonstrate that both the coarse and fine CZ regions can adopt non-unidirectional magnetisations along different interfaces due to subtly different Ni concentrations, which we expect will also have been the case among the different metal particles in the silicates for the same reason. Consequently, we would not expect the remanence remaining after AF demagnetisation to 145 mT to be unidirectional.

4.3. Moment magnetometry of silicates from SJN

The SJN silicates contain neither a unidirectional LC or HC component to their remanence. These absences could imply that this meteorite only ever experienced relatively weak fields on its parent body, however, given the particularly poor remanence retention capabilities of these silicates (Section 3.2.1), it is also feasible that they were magnetised on the parent body and have subsequently lost this remanence due to shock or viscous decay over the intervening billions of years (Tikoo et al., 2015). We note that the fast cooling rate of SJN compared to the inferred timescale of field variation (cooling rate of ∼10000 °C/Myr compared to ∼200 kyr variation time) means that we expect the field orientation would have been roughly constant as this meteorite cooled and hence we would anticipate a unidirectional remanence. If the lack of a remanence is due to the absence of a sufficiently intense field, our inferred paleointensity fidelities imply these silicates experienced field intensities <100–1000 μT. Models of dynamo generation (Scheinberg et al., 2016; Neufeld et al., in prep) predict that, during the first ∼200 kyr of solidification when SJN is predicted to have cooled, the IVA parent core could have generated a field with intensities anywhere between 0–∼200 μT field. The absence of an early field is clearly consistent with our paleomagnetic constraints on the silicates. However, a field at the upper end of this predicted range may also be consistent with our paleointensity constraints on the silicates given the effects of the magnetic shielding (Section 4.2) and uncertainties on the nature of the remanence carried by SJN.

5. Significance of IVA iron meteorites for paleomagnetic studies

We chose to investigate inward core solidification by studying the IVA meteorites as they are, to our knowledge, the most likely samples available that experienced this solidification regime. Although geochemical trends in iron meteorites can provide the direction of core solidification (Yang et al., 2007), there is no way of unambiguously linking rocky or stony-iron meteorites to the same parent body as an iron meteorite family (Goldstein et al., 2009b), making it difficult to assess whether a certain mantle-originating meteorite experienced a field generated during inward solidification. It is also difficult to deduce the direction of core solidification on an intact extraterrestrial body (Williams, 2009; Nimmo, 2009), introducing uncertainties as to whether the remanence carried by meteorites originating from extant asteroids (e.g., the HED meteorites and Vesta; Binzel and Xu, 1993) or present day dynamo field measurements (Anderson et al., 2011) relate to inward core solidification. The IVA meteorites are unique as their geochemical and structural properties indicate that they cooled through their magnetic ordering temperature while their unmantled parent core could still have had molten metal in its interior and hence could have been generating a field.

Traditionally, the iron meteorites have been disregarded paleomagnetically due to their proposed core origin and complicated magnetic mineralogy (Stacey, 1976; Cisowski, 1987; Brecher and Albright, 1977; Funaki and Danon, 1998). To the best of our knowledge, the results in this study are the first successful measurements of ancient dynamo activity from iron meteorites, showing that it is possible to obtain paleomagnetic information from these samples. Despite our observations, we suspect that traditional paleomagnetic techniques applied to bulk metal samples may still struggle to provide accurate ancient field properties, and that iron meteorites that originated from a conventional core geometry are not expected to have cooled through their magnetisation acquisition temperatures in the presence of a dynamo field.

Also, these results are the first to suggest that an asteroid dynamo can produce directionally unstable fields. Directional instabilities on the timescale of 10–100 kyr are an inherent part of the geodynamo, and the observation of this behaviour on a small body reinforces claims that the same fundamental processes drive dynamo activity across rocky bodies (Weiss et al., 2010; Nimmo, 2009). This deduction has key implications for the heat flux of these bodies (Olson et al., 2010) and could provide crucial constraints on their ancient thermal evolution.

6. Conclusions

- Inward core solidification has been hypothesised for various small planetary bodies, although its existence and ability to generate dynamo activity are uncertain. To address these uncertainties, we applied complimentary paleomagnetic techniques to the SJN and Steinbach IVA iron meteorites. This meteorite family has been proposed to originate from an unmantled, inwardly solidifying core, so is the best candidate to have recorded magnetic fields generated during this core solidification regime.
- Silicate inclusions extracted from SJN were found not to contain unidirectional LC or HC components to their magnetisation. Paleointensity fidelity measurements suggest that field intensities $\gtrsim$100–1000 μT were required to impart a reliable remanence in to the HC grains. Given this relatively strong critical intensity, it is possible that the field generated by the IVA parent core was too weak during the period that SJN cooled (first ∼200 kyr of solidification) to impart a reliable remanence. It is also possible that an ancient remanence was imparted and it has subsequently been lost by viscous relaxation or shock.
- XPEEM of matrix metal in Steinbach suggest that this meteorite experienced magnetic fields $\gtrsim$100 μT that exhibited significant orientation changes on a timescale <200 kyr. AF demagnetisation of silicate inclusions extracted from this meteorite do not contain a unidirectional HC component and paleointensity fidelity measurements suggest that some silicate subsamples are capable of acquiring such a remanence at field intensities as weak as a few tens to a few hundreds of μT. Given the relatively quick inferred variation in field orientation compared to the long timescale of Steinbach cooling (cooling rate of 150 °C/Myr at 500 °C), the absence of a HC component is in fact expected and consistent with our XPEEM observations. It is also feasible that the poor paleomagnetic recording fidelity of some Steinbach silicates, coupled with the effects of magnetic shielding, means these silicates experienced field intensities too weak for a reliable remanence to be recorded.
- The presence of a remanence in Steinbach supports an unmantled, inwardly solidifying core origin for this meteorite family, demonstrates that inward core solidification can power dynamo activity (most likely through non-concentric solidification), and establishes that iron meteorites are capable of providing reliable paleomagnetic observations.

Acknowledgements

We acknowledge the Helmholtz-Zentrum Berlin for the use of the synchrotron radiation beamtime at beamline UE49 of BESSY II. The research leading to these results has received funding from the European Research Council under the European Union's Seventh Framework Programme (FP/2007–2013)/ERC grant agreement numbers 320750 and 312284. BPW and JFJB thank the NASA Solar System Exploration Research Virtual Institute (SSERVI), the NASA Solar System Workings Program (grant # NNX15AL62G) and Thomas F. Peterson for support. JFJB thanks the Natural Environment Research Council for financial support. J.H.-A. thanks the MAT2014-53921-R MINECO project. We thank the Natural History Museum, London, and United States National Museum for loaning samples. We also thank Ioan Lascu and Claire Nichols, University of Cambridge, for assistance collecting the XPEEM data, and Huapei Wang, MIT, for assistance collecting the FORC diagrams. We also thank the USNM and NHM for loaning us the meteorite samples used in this study.

Appendix A. Supplementary material

Supplementary material related to this article can be found online at http://dx.doi.org/10.1016/j.epsl.2017.05.026.

References

Anderson, B.J., Johnson, C.L., Korth, H., Purucker, M.E., Winslow, R.M., Slavin, J.A., Solomon, S.C., McNutt, R.L., Raines, J.M., Zurbuchen, T.H., 2011. The global magnetic field of Mercury from MESSENGER orbital observations. Science 333, 1859–1862.

Asphaug, E., Reufer, A., 2014. Mercury and other iron-rich planetary bodies as relics of inefficient accretion. Nat. Geosci. 7, 564–568.

Berndt, T., Muxworthy, A.R., Fabian, K., 2016. Does size matter? Statistical limits of paleomagnetic field reconstruction from small rock specimens. J. Geophys. Res., Solid Earth 121, 15–26.

Binzel, R.P., Xu, S., 1993. Chips off of asteroid 4 Vesta: evidence for the parent body of basaltic achondrite meteorites. Science 260, 186–191.

Brecher, A., Albright, L., 1977. The thermoremanence hypothesis and the origin of magnetization in iron meteorites. J. Geomagn. Geoelectr. 29, 379–400.

Bryson, J.F.J., Church, N.S., Kasama, T., Harrison, R.J., 2014a. Nanomagnetic intergrowths in Fe–Ni meteoritic metal: the potential for time-resolved records of planetesimal dynamo fields. Earth Planet. Sci. Lett. 388, 237–248.

Bryson, J.F.J., Herrero-Albillos, J., Kronast, F., Ghidini, M., Redfern, S.A.T., van der Laan, G., Harrison, R., 2014b. Nanopaleomagnetism of meteoritic Fe–Ni studied using X-ray photoemission electron microscopy. Earth Planet. Sci. Lett. 396, 125–133.
Bryson, J.F.J., Nichols, C.I.O., Herrero-Albillos, J., Kronast, F., Kasama, T., Alimadadi, H., van der Laan, G., Nimmo, F., Harrison, R.J., 2015. Long-lived magnetism from solidification-driven convection on the pallasite parent body. Nature 517, 472–475.
Christensen, U.R., 2015. Iron snow dynamo models for Ganymede. Icarus 247, 248–259.
Cisowski, S.M., 1987. Magnetism of Meteorites. Geomagnetism, vol. 2. Academic Press, New York.
Fearn, D.R., Loper, D.E., 1981. Compositional convection and stratification of earth's core. Nature 289, 393–394.
Funaki, M., Danon, J., 1998. Characteristics of natural remanent magnetization of Nova Petropolis iron meteorite (II). Antarct. Meteor. Res. 11, 189–201.
Gattacceca, J., Suavet, C., Rochette, P., Weiss, B.P., Winklhofer, M., Uehara, M., Friedrich, J.M., 2014. Metal phases in ordinary chondrites: magnetic hysteresis properties and implications for thermal history. Meteorit. Planet. Sci. 49 (4), 652–676.
Goldstein, J., Yang, J., Kotula, P., Michael, J., Scott, E., 2009a. Thermal histories of IVA iron meteorites from transmission electron microscopy of the cloudy zone microstructure. Meteorit. Planet. Sci. 44 (3), 343–358.
Goldstein, J.I., Scott, E.R.D., Chabot, N.L., 2009b. Iron meteorites: crystallization, thermal history, parent bodies, and origin. Chem. Erde - Geochem. 69 (4), 293–325.
Harrison, R.J., Feinberg, J.M., 2008. FORCinel: an improved algorithm for calculating first-order reversal curve distributions using locally weighted regression smoothing. Geochem. Geophys. Geosyst. 9, Q05016.
Hauck, S.A., Aurnou, J.M., Dombard, A.J., 2006. Sulfur's impact on core evolution and magnetic field generation on Ganymede. J. Geophys. Res. 111, E09008.
Kirschvink, J.L., 1980. The least-squares line and plane and the analysis of paleomagnetic data. Geophys. J. Int. 62, 699–718.
Laneuville, M., Wieczorek, M., Breuer, D., Aubert, J., Morard, G., Ruckriemen, T., 2014. A long-lived lunar dynamo powered by core crystallization. Earth Planet. Sci. Lett. 401, 251–260.
Lappe, S.-C.L.L., Feinberg, J.M., Muxworthy, A., Harrison, R.J., 2013. Comparison and calibration of nonheating paleointensity methods: a case study of using dusty olivine. Geochem. Geophys. Geosyst. 14, 20141.
Matter, A., Delbo, M., Carry, B., Ligori, S., 2013. Evidence of a metal-rich surface for the asteroid (16) Psyche from interferometric observations in the thermal infrared. Icarus 226, 419–427.
McClelland, E., 1996. Theory of CRM acquired by grain growth, and its implications for TRM discrimination and paleointensity determination in igneous rocks. Geophys. J. Int. 126, 271–280.
Neufeld, J.A., Bryson, J.F.J., Nimmo, F., in prep. The top-down solidification of iron asteroids driving dynamo evolution.
Nichols, C.I.O., Bryson, J.F.J., Herrero-Albillos, J., Kronast, F., Nimmo, F., Harrison, R.J., 2016. Pallasite paleomagnetism: quiescence of a core dynamo. Earth Planet. Sci. Lett. 441, 103–112.
Nimmo, F., 2009. Energetics of asteroid dynamos and the role of compositional convection. Geophys. Res. Lett. 36, L10210.
Olson, P., Christensen, U.R., 2006. Dipole moment scaling for convection-driven planetary dynamos. Earth Planet. Sci. Lett. 250, 561–571.
Olson, P.L., Coe, R.S., Driscoll, P.E., Glatzmaier, G.A., Roberts, P.H., 2010. Geodynamo reversal frequency and heterogeneous core–mantle boundary heat flow. Phys. Earth Planet. Inter. 180, 66–79.
Reisener, R., Goldstein, J., 2003. Ordinary chondrite metallography: Part 2. Formation of zoned and unzoned metal particles in relatively unshocked H, L, and LL chondrites. Meteorit. Planet. Sci. 38 (11), 1679–1696.
Ruckriemen, T., Breuer, D., Spohn, T., 2015. The Fe snow regime in Ganymede's core: a deep-seated dynamo below a stable snow zone. J. Geophys. Res., Planets 120, 1095–1118.
Ruzicka, A., Hutson, M., 2006. Differentiation and evolution of the IVA meteorite parent body: clues from pyroxene geochemistry in the Steinach stony–iron meteorite. Meteorit. Planet. Sci. 41 (12), 1959–1987.
Scheinberg, A.L., Elkins-Tanton, L.T., Schubert, G., Bercovici, D., 2016. Core solidification and dynamo evolution in a mantle-stripped planetesimal. J. Geophys. Res., Planets 121, 2–20.
Smirnov, A.V., Tarduno, J.A., 2005. Thermochemical remanent magnetization in Precambrian rocks: are we sure the geomagnetic field was weak? J. Geophys. Res. 110, B06103.
Stacey, F.D., 1976. Paleomagnetism of meteorites. Annu. Rev. Earth Planet. Sci. 4, 147–157.
Stephenson, A., 1993. Three-axis static alternating field demagnetization of rocks and the identification of natural remanent magnetization, gyroremanent magnetization, and anisotropy. J. Geophys. Res. 98, 373–381.
Tarduno, J.A., Cottrell, R.D., Nimmo, F., Hopkins, J., Voronov, J., Erickson, A., Blackman, E., Scott, E.R.D., Mckinley, R., 2012. Evidence for a dynamo in the main group pallasite parent body. Science 338 (6109), 939–942.
Tauxe, L., Staudigel, H., 2004. Strength of the geomagnetic field in the Cretaceous Normal Superchron: new data from submarine basaltic glass of the Troodos Ophiolite. Geochem. Geophys. Geosyst. 5 (2), Q02H06.
Tikoo, S.M., Gattacceca, J., Swanson-Hysell, N.L., Weiss, B.P., 2015. Preservation and detectability of shock-induced magnetization. J. Geophys. Res., Planets 120, 1461–1475.
Tikoo, S.M., Weiss, B.P., Buz, J., Lima, E.A., Shea, E.K., Melo, G., Grove, T.L., 2012. Magnetic fidelity of lunar samples and implications for an ancient core dynamo. Earth Planet. Sci. Lett. 337, 93–103.
Tikoo, S.M., Weiss, B.P., Cassata, W.S., Shuster, D.L., Gattacceca, J., Lima, E.A., Suavet, C., Nimmo, F., Fuller, M.D., 2014. Decline of the lunar core dynamo. Earth Planet. Sci. Lett. 404, 89–97.
Uehara, M., Gattacceca, J., Leroux, H., Jacob, D., van der Beek, C.J., 2011. Magnetic microstructures of metal grains in equilibrated ordinary chondrites and implications for paleomagnetism of meteorites. Earth Planet. Sci. Lett. 306 (3–4), 241–252.
Wang, H., Weiss, B.P., Bai, X.-N., Downey, B.G., Wang, J., Wang, J., Suavet, C., Fu, R.R., Zucolotto, M.E., 2017. Lifetime of the solar nebula constrained by meteorite paleomagnetism. Science 355, 623–627.
Wasson, J.T., Matsunami, Y., Rubin, A.E., 2006. Silica and pyroxene in IVA irons; possible formation of the IVA magma by impact melting and reduction of L-LL-chondrite materials followed by crystallization and cooling. Geochim. Cosmochim. Acta 70, 3149–3172.
Weisberg, S., 1985. Applied Linear Regression. John Wiley and Sons, New York.
Weiss, B.P., Gattacceca, J., Stanley, S., Rochette, P., Christensen, U.R., 2010. Paleomagnetic records of meteorites and early planetesimal differentiation. Space Sci. Rev. 152, 341–390.
Weiss, B.P., Tikoo, S.M., 2014. The lunar dynamo. Science 346, 1246753.
Williams, Q., 2009. Bottom-up versus top-down solidification of the cores of small solar system bodies: constraints on paradoxical cores. Earth Planet. Sci. Lett. 284, 564–569.
Yang, C.-W., Williams, D.B., Goldstein, J.I., 1996. A revision of the Fe–Ni phase diagram at low temperatures (<400 °C). J. Phase Equilib. 17 (6), 522–531.
Yang, J., Goldstein, J.I., 2005. The formation of the Widmanstätten structure in meteorites. Meteorit. Planet. Sci. 40 (2), 239–253.
Yang, J., Goldstein, J.I., Scott, E.R.D., 2007. Iron meteorite evidence for early formation and catastrophic disruption of protoplanets. Nature 446 (7138), 888–891.
Yang, J., Goldstein, J.I., Scott, E.R.D., 2010. Main-group pallasites: thermal history, relationship to IIIAB irons, and origin. Geochim. Cosmochim. Acta 74, 4471–4492.